RSC Advances

PAPER

View Article Online
View Journal | View Issue

Cite this: *RSC Adv.*, 2025, **15**, 49751

Rational design of highly dispersed ultra-small Ru nanoparticles on MgO–Al_2O_3 for efficient and selective aromatic hydrogenation

Yongjun Wang,[ab] Cheng Han, *[a] Xiaohan Wu,[a] Minglin Xiang,[b] Tao Liu,[a] Xiaoshan Zhang,[a] Bing Wang[a] and Yingde Wang *[a]

Continuous selective hydrogenation of aromatic compounds exhibits broad application prospects, serving as a key process for the synthesis of high-value-added polymer monomers and pharmaceutical intermediates. The fabrication of heterogeneous catalysts being even more critical to enabling this continuous process. Herein, the traditional preparation protocol of supported Ru-based catalysts was systematically optimized, resulting in a novel Ru/MgO–Al_2O_3 catalyst with highly dispersed, ultra-small Ru nanoparticles. This innovative catalyst demonstrated exceptional catalytic activity and selectivity for the hydrogenation of phenolic compounds to alicyclic alcohols, with preferential aromatic ring hydrogenation and suppressed C–O/C–C bond hydrogenolysis. Leveraging this insight, additional studies revealed its comparable outstanding activity and selectivity in the hydrogenation of aromatic esters and ethers to corresponding alicyclic derivatives. This discovery is critical for realizing aromatic hydrocarbon saturation and non-aromatic residue in chemical processes, thereby endowing it with profound significance in the field of chemical manufacturing.

Received 6th November 2025
Accepted 3rd December 2025

DOI: 10.1039/d5ra08531d

rsc.li/rsc-advances

1. Introduction

The selective hydrogenation of aromatic compounds represents a crucial route for producing aliphatic derivatives, which serve as key starting materials for polymers, resins, dyes, and fine chemicals.[1–3] As is well established, the intrinsic structure of a molecule determines its properties and applications. During the hydrogenation of aromatic compounds, the saturation of aromatic rings induces structural changes. These changes are reflected not only in physicochemical characteristics (*e.g.*, mechanical strength, thermal stability, reactivity) but also in enhanced safety profiles of materials derived from such hydrogenated intermediates, which pose no toxic hazards to humans. Substances such as *o*-cresol, bisphenol A (BPA) and hydroquinone are widely used in resin synthesis. However, the unsaturated aromatic groups are commonly labeled as an endocrine disruptor,[4–6] which can cause skin allergy, reproductive toxicity and risk of teratogenicity.[7–9] For instance, resins derived from hydrogenated bisphenol A (HBPA) exhibit stable anti-yellowing properties and biocompatibility, enabling their widespread high-end applications. Traditional phthalate plasticizers face significant challenges under such as the REACH regulations, which mandates residual benzene ring content <50 ppm in human-contact plasticizers.[10–12] Notably, aromatic ring saturation *via* hydrogenation offers a viable route to fabricate novel eco-friendly plasticizers meeting this stringent requirement.

Hydrogenation reaction modes mainly include batch reactor hydrogenation and continuous hydrogenation. Selective continuous hydrogenation serves as an environmentally friendly, clean, and 100% atom-economical synthetic approach, holding critical importance in chemical industrial production.[13] Relative to traditional batch hydrogenation processes, it minimizes emissions of hydrogen-containing organic waste gases while enabling precise process control, stable product quality, and simplified operation. These advantages are prominently observed in the synthesis of high-value-added fine chemicals, pharmaceutical intermediates, and human health-related research.[14] Nevertheless, the heterogeneous selective catalysts are even pivotal to this process; catalyst mechanical strength, physicochemical properties, active metal characteristics (type, content, size, dispersion), and preparation methods all exert notable effects on catalytic performance.[15–17] Studies have demonstrated that the dispersion and particle size of the active metal play a crucial role in the activity of hydrogenation catalysts,[18] while the acidity of the support surface is of great importance for the selectivity towards target products during the hydrogenation process. Catalysts commonly employed for the hydrogenation of aromatic compounds include Ni, Co, Ru, Rh, Pd, and Pt,[19–22] while typical supports are activated carbon, Al_2O_3, SiO_2, and TiO_2. Notably, Ru-based[23–25] catalysts exhibit superior aromatic hydrogenation activity while also being the most cost-

[a]*Science and Technology on Advanced Ceramic Fibers and Composites Laboratory, College of Aerospace Science and Engineering, National University of Defense Technology, Changsha 410073, P.R.China. E-mail: wangyingde@nudt.edu.cn; hancheng@nudt.edu.cn*

[b]*Hunan Changlian Newmaterial Technology CO., Ltd, Yueyang 414012, P.R.China*

effective among noble metal catalysts, thus offering great potential for reducing catalyst production costs in industrial applications. Al_2O_3 is widely used in petrochemicals owing to its stable physicochemical properties and favorable pore structure.[26]

Taking all the aforesaid into account, Ru was selected as the catalytic active center and Al_2O_3 as the catalyst support in this study. Under the continuous fixed-bed hydrogenation mode, the catalytic performance of Ru/MgO–Al_2O_3 catalysts for the hydrogenation of various aromatic compounds was systematically investigated *via* the optimization of catalyst preparation methods and the regulation of support acidity by MgO modification.[27,28] Their physicochemical properties were comprehensively characterized *via* XRD, H_2-TPR, TEM, XPS, NH_3-TPD, and ICP-AES, with results correlated to hydrogenation performance. Initially, catalyst precursors were treated with NaOH to form easily reducible oxides, lowering reduction temperature and facilitating the ultra-small Ru nanoparticle formation. Based on this observation, subsequent MgO modification[29] tailored Lewis acidity, adjusted the electron density between the active metal and support, and ultimately produced a Ru-based catalyst with highly dispersed, ultra-small nanoparticles. Due to MgO-regulated Lewis acidity, the catalyst suppressed C–O/C–C bond hydrogenolysis. Further tests showed it also exhibited exceptional activity and selectivity in hydrogenating aromatic esters, aromatic ethers, and biomass-derived furans to corresponding alicyclic products.[30] This finding is critical for achieving aromatic saturation and non-aromatic residue in chemical processes, holding profound significance for chemical manufacturing.

2. Experimental section

2.1 Materials

All chemicals utilized in the experiments are of analytical reagent (AR) grade purity and used without additional purification. Ruthenium(III) chloride hexahydrate ($RuCl_3 \cdot 6H_2O$, Ru ≥ 37.0%) is purchased from Shaanxi Kaida Chemical Engineering Co., Ltd (Baoji, China). Sodium hydroxide (NaOH, 96.0%), ethanol (≥99.5%), isopropanol (≥99.7%), methylcyclohexane (≥99.5%), magnesium nitrate hexahydrate ($Mg(NO_3)_2 \cdot 6H_2O$, 99.0%) and hydrazine hydrate (N_2H_4 ≥ 80.0%) are acquired from China National Pharmaceutical Group Corporation (Shanghai, China). Aluminum oxide (≥99.0%) is obtained from Sinopec Catalyst Co., Ltd (Yueyang, China). Reactants used in the experiment include hydroquinone(≥99.0%), *o*-cresol(≥99.0%) are obtained from Sinopharm Group (Beijing, China), whereas bisphenol A (≥99.5%) is supplied by Sinopec Mitsui Chemical Co., Ltd (Shanghai, China), diisooctyl phthalate (DOP ≥ 99.5%) and diisononyl phthalate (DINP ≥ 99.5%) are supplied by Formosa Plastics Group (Taiwan, China).

2.2 Catalyst preparation

The supported Ru/Al_2O_3 catalysts were synthesized *via* the excessive impregnation method, and the detailed preparation procedure described as following. Firstly, the catalyst support Al_2O_3 was dried at 120 °C for 12 hours, then impregnated with $RuCl_3 \cdot 6H_2O$ solution at 85 °C for 8 h. Subsequently, the ruthenium catalyst precursor was filtered and dried at 120 °C for 24 h. The catalysts were categorized into different types according to the post-treatment methods applied to the ruthenium catalyst precursor, as illustrated in Fig. 1. Without any prior treatment, catalyst precursors are directly reduced in H_2 atmosphere to yield the catalyst designated as Ru/Al_2O_3-I. The catalyst precursor, first calcined at 450 °C and then reduced in H_2 atmosphere to yield the catalyst designated as Ru/Al_2O_3-II. Washing the catalyst precursor with sodium hydroxide solution and then dried overnight prior to H_2 reduction, which is labeled as Ru/Al_2O_3-III. The catalyst, which is reduced using hydrazine hydrate with the same pre-treated process of Ru/Al_2O_3-III is marked as Ru/Al_2O_3-IV. On the other hand, the MgO modified

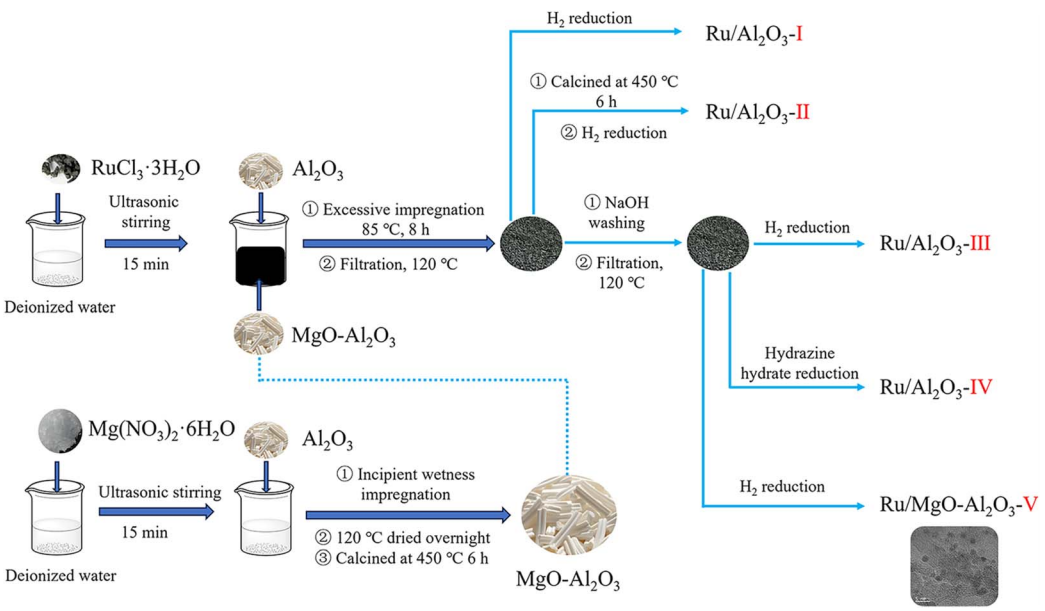

Fig. 1 The flowchart for catalyst preparation process.

catalyst support is prepared by incipient wetness impregnation of $Mg(NO_3)_2 \cdot 6H_2O$ solution with Al_2O_3, then dried at 120 °C for 8 hours and calcined at 450 °C for 6 hours. While the supported $Ru/MgO–Al_2O_3$ catalyst is prepared by excessive impregnation, and the detailed preparation procedure is same to Ru/Al_2O_3-III, and the MgO modified catalyst is designated as $Ru/MgO–Al_2O_3$-V. It is worth noting that the effects of the content of active metal Ru and MgO have been thoroughly examined in our previously published research.[31] Studies also revealed that with a progressive increase in Ru loading, the particle size of Ru (the active component) exhibits a gradual enlargement, accompanied by the aggregation of Ru particles.[32–34] This aggregation-induced decline in the dispersion of active sites ultimately compromises the catalytic activity of the catalyst. For the current study, active metal ruthenium and MgO are present at a content of 3.0 weight percent (wt.%).

2.3 Catalyst characterization

Powder X-ray diffraction (XRD) measurements were performed using an Ultima IV diffractometer, employing Ni-filtered Cu Kα radiation (40 kV, 50 mA), catalysts were scanned over a 2θ range of 10–80° at a step size of 0.02°. The Specific surface area and pore volume of the catalysts were determined *via* dynamic nitrogen adsorption at −196 °C, using a Micromeritics ASAP2400 instrument. Transmission electron microscopy (TEM) images were obtained with a Joel JEM-F200 microscope. For TEM sample preparation: the synthesized catalyst powder was diluted in ethanol, ultrasonicated for 5 minutes, and droplets of the resulting suspension were deposited onto a copper grid. The grid was then dried overnight in a vacuum oven at 100 °C. Particle size distribution statistics were calculated using the Nano Measurer image analysis software. H_2 chemisorption, temperature-programmed reduction (TPR), and NH_3 temperature-programmed desorption (NH_3-TPD) experiments were conducted on a Micromeritics Autochem II 2920 system. X-ray photoelectron spectroscopy (XPS) measurements were carried out with a Thermo Scientific K-Alpha spectrometer, equipped with a hemispherical electron analyzer and a 300 W Al Kα X-ray source ($E = 1486.4$ eV). For XPS analysis: the powder sample was mounted on double-sided copper adhesive tape, placed on a sample rod in the pretreatment chamber, and subsequently transferred to the analysis chamber. Prior to spectral collection, the sample was held in the analysis chamber until a residual pressure of approximately 5×10^{-7} Nm^{-2} was achieved. Narrow-scan spectra for target elements were recorded at a pass energy of 50 eV. The actual metal ruthenium loading in the catalysts were determined by Inductively Coupled Plasma Optical Emission Spectrometer (ICP-OES), using an Agilent 5110 instrument.

2.4 Catalytic hydrogenation evaluation

The hydrogenation reaction testing for the synthesized catalysts is carried out on a fixed-bed reactor shown in Fig. 2. Catalysts are loaded into the middle section of the reactor, with inert packing material placed above and below, the inner diameter of the reactor is 22 mm, and the fixed-bed reactor is heated using an electric heater. Prior to the hydrogenation reaction, catalysts are all pretreated under hydrogen atmosphere at 80–250 °C for 8 h. The reaction feed is pumped at a controlled flow rate, mixed with hydrogen, and preheated before entering the catalyst-packed reactor. The hydrogenated mixtures are quantitatively analyzed using a gas chromatograph equipped with a 30 m SE-54 capillary column to evaluate the performance of the synthesized catalysts. Meanwhile, product identification is conducted *via* gas chromatography-mass spectroscopy (GC-MS) on an Agilent 7890 C instrument.

Feedstock conversion (Conv./%) and selectivity (Sel./%) toward the target product are most critical metrics for assessing the overall performance of the catalyst, which are calculated as follows:

$$\text{Conv.}(\%) = \frac{\text{mole of feedstock consumed}}{\text{initial mole of feedstock}} \times 100\% \quad (1)$$

$$\text{Sel.}(\%) = \frac{\text{mole of target product}}{\text{mole of all products formed}} \times 100\% \quad (2)$$

The Weight Hourly Space Velocity (WHSV) is a critical parameter for characterizing a catalyst's processing capacity. This important parameter reflects the catalyst's capacity to process reactants, representing the amount of raw material that a specified quantity of catalyst can convert within a set time-frame. It is calculated as follows:

$$\text{WHSV.}(h^{-1}) = \frac{\text{the mass flow rate of the feedstock } (\text{kg h}^{-1})}{\text{the mass of the catalyst(kg)}} \quad (3)$$

The hydrogen–oil molar ratio represents the molar ratio of H_2 to the raw material per unit time, and it is precisely measured using a flowmeter during the experiment. It is also an important parameter of the hydrogenation reaction, which is calculated as follows:

$$H/O = \frac{\text{mole of hydrogen}(H_2)}{\text{mole of the feedstock}} \quad (4)$$

3. Results and discussion

3.1 Characterization of catalysts

The porous parameters of these materials calculated from the isotherms, and the size of ruthenium active centers nanoparticles of the studied catalysts observed by TEM micrographs are compiled in Table 1. As summarized in Table 1, the Al_2O_3 support exhibits a BET surface area (S_{BET}) of 210 m^2 g^{-1}, a total pore volume (PV) of 0.68 cm^3 g^{-1}, and an average pore diameter of 10.24 nm. Modifying the support with MgO exerted no appreciable influence on its pore size and pore volume. Nevertheless, a slight decrease in specific surface area is observed, which may be attributed to the deposition of MgO nanoparticles (causing partial pore blockage) and interactions between Al_2O_3 support and MgO.[35] As showed in Fig. S1, with the exception of

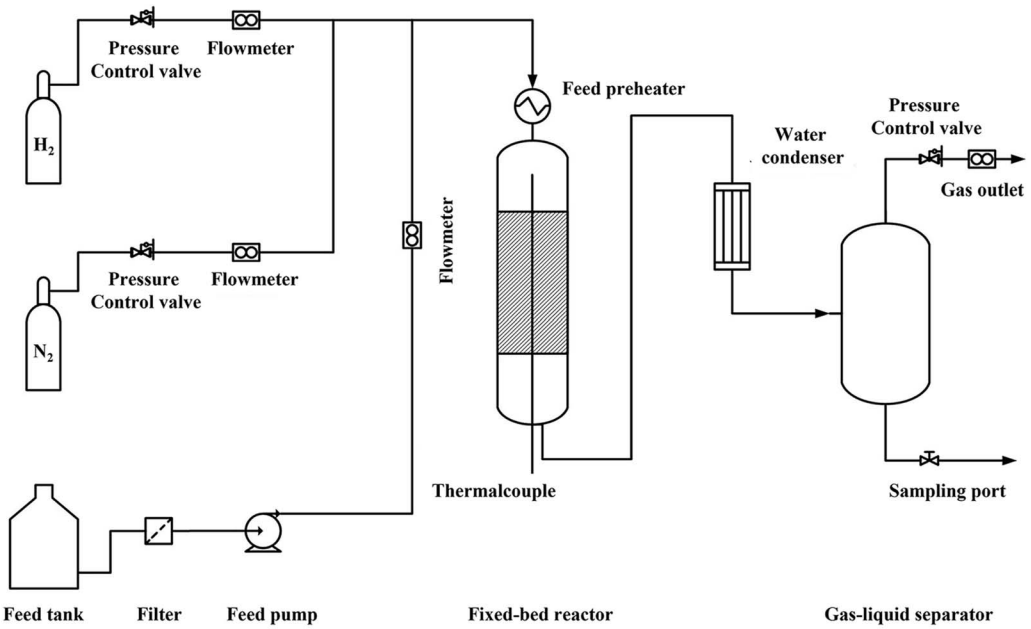

Fig. 2 Process flow diagram for catalyst hydrogenation reaction testing.

Ru/Al_2O_3-II, the catalysts exhibited negligible changes in pore volume relative to the catalyst support, accompanied by a slight reduction in pore size and a substantial increase in specific surface area. Following NaOH treatment, the Ru/Al_2O_3-III, Ru/Al_2O_3-IV, and $Ru/MgO–Al_2O_3$-V catalysts exhibited notably higher specific surface areas compared with the untreated Ru/Al_2O_3-I and Ru/Al_2O_3-II catalysts, which is 225 $m^2\ g^{-1}$ and 210 $m^2\ g^{-1}$ respectively. This observation is likely due to the etching action of NaOH on the catalyst support.

The size of the active center Ru was statistically analyzed by transmission electron microscopy, with the results summarized in Table 1. The average Ru nanoparticle diameters for Ru/Al_2O_3-I, Ru/Al_2O_3-II, Ru/Al_2O_3-III, Ru/Al_2O_3-IV, $Ru/MgO–Al_2O_3$-V are 1.86 nm, 7.13 nm, 2.32 nm, 2.09 nm, and 1.72 nm, respectively. It is particularly noteworthy that Ru/Al_2O_3-II exhibits substantially larger Ru nanoparticles compared with the other four catalysts. This is primarily attributed to the sintering and agglomeration of RuO_x species formed during the 450 °C high-temperature calcination of the $RuCl_3$ precursor, leading to an increase in particle size.[36] TEM images further clearly reveal the agglomeration of Ru nanoparticles, showed in Fig. 4b. More notably, the MgO-modified catalyst possesses the smallest active metal particle size and the largest specific surface area, both of which are crucial for improving catalytic performance. This observation can be ascribed to the acid–base property regulation of Al_2O_3 upon MgO modification, which facilitates the formation of highly dispersed Ru nanoparticles[37] and ultimately results in ultra-small Ru particles. Furthermore, literature reports[38–40] indicate that MgO modification diminishes the catalyst's acidity, thereby inhibiting the cleavage of C–OH and C–C bonds. Such inhibition suppresses the generation of diverse hydrogenation by-products, leading to improved selectivity for the target product, which in agreement with subsequent findings. The active metal Ru content and the catalyst's surface density are also shown in Table 1. During the catalyst synthesis, the loading of active ruthenium (Ru) was uniformly

Table 1 Physicochemical properties of the samples

	Pore parameters					
Catalysts	$S_{BET}/m^2\ g^{-1}$	$P_V/cm^{-3}\ g^{-1}$	D/nm	Diameter[a]/nm	Ru[b]/wt.%	$\rho s^c/\mu g\ m^{-2}$
Al_2O_3	210.55	0.68	10.24	—	—	—
MgO/Al_2O_3	205.10	0.66	10.24	—	—	—
Ru/Al_2O_3-I	212.18	0.66	10.05	1.86	2.95	139.03
Ru/Al_2O_3-II	208.78	0.69	10.34	7.13	2.89	138.42
Ru/Al_2O_3-III	223.54	0.67	9.97	2.32	2.86	127.94
Ru/Al_2O_3-IV	225.05	0.65	9.63	2.09	2.84	126.19
$Ru/MgO–Al_2O_3$-V	228.55	0.63	9.57	1.72	2.82	123.39

[a] Calculated from TEM results. [b] Ru content are determined by ICP-AES. [c] Surface density are calculated from Ru content and the surface area of catalysts.

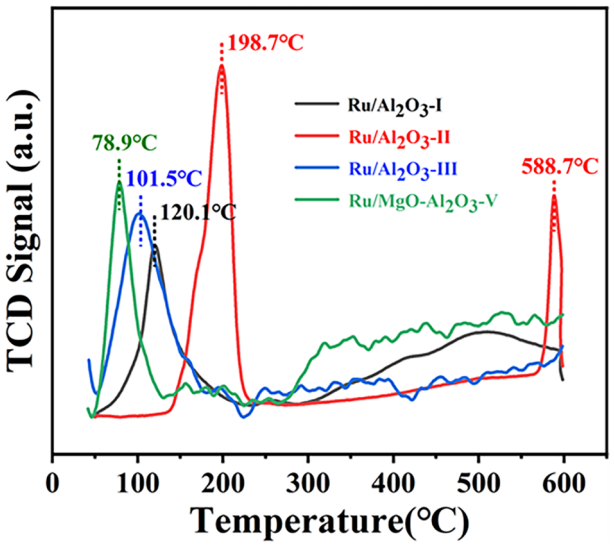

Fig. 3 H_2-TPR patterns of the supported ruthenium catalysts.

controlled at 3 wt.% across all samples. ICP-OES analyses confirmed that the Ru contents in Ru/Al_2O_3-I and Ru/Al_2O_3-II—prepared without precursor pretreatment—were marginally higher than those in catalysts derived from NaOH-pretreated precursors (Ru/Al_2O_3-III, Ru/Al_2O_3-IV, $Ru/MgO–Al_2O_3$-V). This discrepancy arises primarily from partial leaching of the active metal during NaOH washing. Additionally, the surface area densities of these catalysts fell within the range of 125–139 μg m^{-2}. Notably, the catalysts prepared without NaOH pretreatment exhibited a slightly lower specific surface area, which consequently led to a moderately higher surface area density relative to their counterparts.

X-ray diffraction (XRD) serves as a key analytical technique for obtaining critical insights into material composition and the atomic/molecular-level structural or morphological characteristics. The crystal structure of the catalyst support and supported ruthenium catalysts are probed by XRD, which showed in Fig. S2. The XRD patterns of Al_2O_3 and MgO/Al_2O_3 are nearly identical, with only the characteristic reflections of Al_2O_3 being observed. No distinct diffraction peaks attributable to MgO are detected, primarily due to the high dispersion and relatively low loading of MgO. With the exception of Ru/Al_2O_3-II, the XRD patterns of the various catalysts reveal that there are no distinct diffraction peaks corresponding to the metallic ruthenium phase are observed for the other catalysts. This observation suggests that ruthenium is highly dispersed on the support, which is well consistent with the phenomenon observed in the TEM images showed in Fig. 4a and c–e. In contrast to the catalysts reduced under a hydrogen atmosphere, the X-ray diffraction pattern of the Ru/Al_2O_3-IV catalyst reduced with hydrazine hydrate exhibits two relatively weak characteristic peaks of RuO_2 observed at $2\theta = 29.3$ (110), 53.8(211),[41] in agreement with the JCPDS file (PDF file # 40-1290). This result indicating the presence of partially unreduced ruthenium oxide under this reduction protocol. Nevertheless, a distinct characteristic peak attributed to Ru metal observed in the XRD spectrum of the Ru/Al_2O_3-II catalyst at $2\theta = 44.0°$, which can be indexed to the (101) lattice plane of metallic ruthenium with a hexagonal close-packed (hcp) structure, in agreement with the JCPDS file (PDF file # 06-0663). This observation is fully

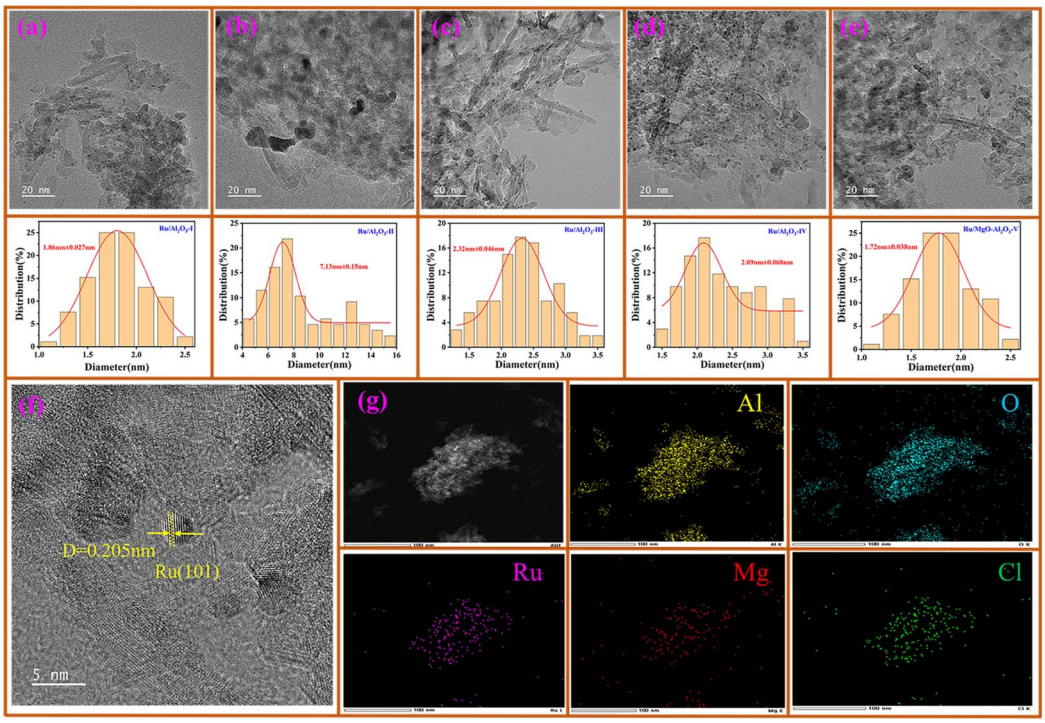

Fig. 4 TEM micrographs of the supported ruthenium catalysts: Ru/Al_2O_3-I (a), Ru/Al_2O_3-II (b), Ru/Al_2O_3-III (c), Ru/Al_2O_3-IV (d) and $Ru/MgO–Al_2O_3$-V (e and f). HAADF-STEM images of $Ru/MgO–Al_2O_3$-V (f) and EDS mapping images of the $Ru/MgO–Al_2O_3$-V (g).

consistent with the findings from H_2 temperature-programmed reduction (H_2-TPR) and transmission electron microscopy (TEM) analyses, which showed in Fig. 3 and 4b. TEM images clearly reveal sintering and agglomeration of metallic ruthenium, while the H_2-TPR profile shows that this catalyst exhibits the highest reduction temperature. These results collectively indicate that the ruthenium catalyst prepared *via* precursor calcination possesses low dispersion and relatively large particle sizes.

Furthermore, the Ru/Al_2O_3-II, Ru/Al_2O_3-IV, Ru/MgO–Al_2O_3-V catalysts obtained after the pretreatment step involving washing the catalyst precursor with NaOH solution exhibited two distinct diffraction peaks around 20.0°, which are characteristic of $NaAlO_2$.[42] This phase is primarily generated *via* the reaction between NaOH and the catalyst support Al_2O_3 during the pretreated process. Notably, for the catalyst prepared using the MgO-modified support, the intensity of these $NaAlO_2$ peaks is significantly reduced. This observation may be attributed to the inhibiting effect of MgO on $NaAlO_2$ formation, or alternatively, to the formation of $MgAl_2O_4$ ref. 43 spinel at overlapping diffraction positions, leading to peak broadening and attenuation in the XRD pattern. $NaAlO_2$ and $MgAl_2O_4$ are both alkaline in nature, and their formation can effectively reduce the acidity of the catalyst support. Moreover, these phases exhibit relatively high chemical stability, which may contribute to enhancing the overall stability of the catalyst.[44,45]

H_2-TPR analyses are conducted to investigate the reducibility of the supported ruthenium catalysts, which can significantly influence catalytic performance. With the exception of Ru/Al_2O_3-II, a single well-defined hydrogen consumption peak below 150 °C was observed for the prepared catalysts Ru/Al_2O_3-I, Ru/Al_2O_3-III and Ru/MgO–Al_2O_3-V (Fig. 3). Studies[46,47] have shown that the reduction peaks appearing below 200 °C in Ru-based supported catalysts are universally assigned to the characteristic reduction of surface RuO_x species. In contrast, in the case of Ru/Al_2O_3-II catalyst displays two distinct reduction peaks: one centered near 200 °C (198.7 °C) and another at a higher temperature of 588.7 °C. Complementary TEM characterization results provide insight into this unique reduction behavior: the active RuO_x species in Ru/Al_2O_3-II undergo significant sintering and agglomeration,[48,49] resulting in larger RuOx particle sizes. The increased particle size, coupled with enhanced metal-support interaction (MSI) between Ru species and the Al_2O_3 support, elevates the reduction energy barrier for these RuO_x aggregates—manifested as the reduction peak at 198.7 °C. Notably, the high-temperature reduction peak at 588.7 °C is proposed to originate from a specific Ru-containing species formed during the 450 °C calcination step. It is hypothesized that large RuO_x particles, derived from the catalyst precursor, interact strongly with the Al_2O_3 support to form a stable Ru–O–Al interfacial structure. This Ru–O–Al species exhibits high thermal stability, requiring a much higher reduction temperature to break the strong Ru–O–Al bonds and achieve complete reduction to metallic Ru^0.

Among these prepared catalysts, the variation trend of Ru species reduction temperatures (Ru/MgO–Al_2O_3-V < Ru/Al_2O_3-III < Ru/Al_2O_3-I < Ru/Al_2O_3-II) implies a corresponding descending order of H_2 dissociation capability for the catalysts, *i.e.*, Ru/MgO–Al_2O_3-V > Ru/Al_2O_3-III > Ru/Al_2O_3-I > Ru/Al_2O_3-II. This sequence of H_2 dissociation capability is well-correlated with the catalytic activity results presented in Table 3, where an identical activity order (Ru/MgO–Al_2O_3-V > Ru/Al_2O_3-III > Ru/Al_2O_3-I > Ru/Al_2O_3-II) is observed. Notably, the Ru/MgO–Al_2O_3-V catalyst which modification of MgO results in a significant decrease to 78.9 °C. In our previously published works,[31] a systematic investigation was conducted to elucidate the correlation between MgO loading (0–5 wt%) and the reduction behavior of RuO_x for the Ru/MgO–Al_2O_3 catalysts. Results showed that the reduction temperature decreased initially before increasing with the incorporation of MgO into the catalyst support, with the lowest reduction temperature attained at a MgO loading of 3 wt%. This pronounced reduction temperature lowering is primarily ascribed to MgO facilitates the dispersion of active Ru species, promoting the formation of ultra-small Ru nanoparticles, which substantially lowers the energy barrier for H_2-induced reduction. Furthermore, MgO modulates the electronic state of the active Ru species to a certain extent—likely *via* electron transfer at the Ru–MgO interface or the induction of a local electron-rich environment around Ru sites—which further weakens the Ru–O bond strength and thus contributes to the reduced reduction temperature.[50] The TEM results showed that the Ru/MgO–Al_2O_3-V catalyst presented the minimum size of 1.72 nm among the prepared ruthenium catalysts, which is well consistent with the above observation results.

Ammonia Temperature-Programmed Desorption (NH_3-TPD) is a well-established characterization technique for probing the surface acid properties of catalytic materials,[51] Fig. S3 presented the NH_3-TPD patterns of the studied catalysts. The as-fabricated catalysts display three distinct characteristic signals at 100 °C, 250 °C and 400 °C, assigned to weak, medium-strong, and strong acid sites, respectively.[52] The catalyst supports Al_2O_3 and MgO/Al_2O_3 exhibited signal peaks solely at 100 °C and 400 °C, whereas the 250 °C signal in the catalyst can attributed to ruthenium (Ru) catalyst formation.[53] Compared with catalyst support's intrinsic acidity, Ru/Al_2O_3-I and Ru/Al_2O_3-II which prepared *via* direct H_2 reduction and post-calcination of $RuCl_3$ precursor exhibited significantly higher acidity, primarily due to Lewis acid HCl introduced during synthesis. NaOH washing of the precursor induces a marked acidity decline for Ru/Al_2O_3-III, whereas MgO modification affords the lowest acidity for Ru/MgO–Al_2O_3-V. For the hydrazine hydrate-reduced Ru/Al_2O_3-IV catalyst, three distinct peaks in 100–300 °C range stems mainly from the decomposition of residual hydrazine hydrate during characterization. Generally, NaOH pretreatment decreases catalyst acidity, and MgO modification further diminishes its intrinsic acidity. This reduced acidity may effectively inhibits C–C and C–OH bond cleavage in the hydrogenation process, thus improving selectivity toward the aromatic ring-saturated target product.[54]

Transmission electron microscopy (TEM) images are acquired to characterize the morphology and particle size distribution of the as-prepared catalyst, as shown in Fig. 4. Notably, all catalysts except Ru/Al_2O_3-IV exhibit uniform

dispersion of active metal nanoparticles on the Al_2O_3 support, with an average size of ~2.0 nm. As can be observed from Fig. 4a, c and d, the average particle size of ruthenium metal for Ru/Al_2O_3-I, Ru/Al_2O_3-III and Ru/Al_2O_3-IV is 1.86 nm, 2.32 nm and 2.09 nm, respectively. For the Ru/Al_2O_3-IV catalyst, Ru particles show a significant size increase to 7.13 nm, with distinct metal clusters visible in TEM images, primarily attributed to high-temperature sintering during preparation. Notably, the Ru/MgO–Al_2O_3-V catalyst exhibits the smallest average Ru particle size (1.72 nm), suggesting that MgO modification promotes Ru active site dispersion, thereby forming ultra-small Ru nanoparticles and enhancing catalytic activity. More interestingly, the average particle size of ruthenium for the prepared catalysts correlates positively with their H_2-TPR reduction temperatures: larger particles necessitate higher reduction temperatures.

X-ray photoelectron spectroscopy (XPS) is employed to characterize the valence and electronic properties of Ru for the target catalysts, shown in Fig. 5. To avoid overlap between Ru $3d_{3/2}$ and C 1s peaks at 284.8 eV, Ru 3p XPS spectra were analyzed to determine the valence states and electronic properties of Ru.[55] The Ru 3p spin–orbit splits into Ru $3p_{3/2}$ and Ru $3p_{1/2}$, the fitted peaks at 462.4 eV, 484.1 eV are attributed to the Ru (0) species,[56] while the peaks at higher binding energies (466.7, 488.3 eV) correspond to Ru(IV).[57] XPS qualitative analysis results for the catalysts are summarized in Table 2. Despite the nearly consistent total content of active Ru species during catalyst preparation, results observed from Table 2 reveal that the peak area and the distributions of Ru (0) and Ru(IV) vary among the samples. The Ru (0)/Ru(IV) peak area ratio follows an identical order in both $3p_{3/2}$ and Ru $3p_{1/2}$ regions: Ru/MgO–Al_2O_3-V > Ru/Al_2O_3-III > Ru/Al_2O_3-I > Ru/Al_2O_3-II > Ru/Al_2O_3-IV. Notably, Ru/MgO–Al_2O_3-V displays the highest ratios (5.97 and 4.93, respectively), corroborating its elevated content of reduced metallic Ru and enhanced reducibility—consistent with its lowest H_2-TPR reduction temperature and the ultra-small, highly dispersed particles observed *via* TEM images. In contrast, the hydrazine hydrate-reduced catalyst Ru/Al_2O_3-IV exhibits the lowest Ru (0)/Ru(IV) ratios (2.4 and 2.19), attributed to incomplete reduction during synthesis. Ru/Al_2O_3-II also shows relatively low ratios, correlating with its large particle size and significant aggregation. XPS characterization offers profound insights into the surface valence distribution of the catalysts, with all findings consistent with H_2-TPR and TEM results.

3.2 Catalytic performance

The selective hydrogenation of *o*-cresol is performed on a fixed-bed reactor to systematically evaluate the catalytic activity and selectivity of the catalysts, with the results compiled in Table 3. The desired product is aromatic ring-saturated *o*-methylcyclohexanol. During hydrogenation, C–C and C–OH bond cleavage-induced side reactions take place, generating methylcyclohexane, cyclohexanol, and cyclohexane as byproducts. Notably, *o*-methylcyclohexanone is identified in the hydrogenation products under reduced catalyst activity, which is likely resulting from the isomerization of the semi-hydrogenation intermediate cyclohexenol. As clearly reflected in Table 3, catalysts exhibit a hydrogenation activity order of Ru/MgO–Al_2O_3-V > Ru/Al_2O_3-III > Ru/Al_2O_3-I > Ru/Al_2O_3-II > Ru/Al_2O_3-IV, well consistent with the trends deduced from physicochemical characterizations (H_2-TPR, XPS, TEM). Their selectivity towards the target product *o*-methylcyclohexanol follows a distinct sequence: Ru/MgO–Al_2O_3-V > Ru/Al_2O_3-IV > Ru/Al_2O_3-III > Ru/Al_2O_3-II > Ru/Al_2O_3-I, which correlates positively with the catalyst basicity as probed by NH_3-TPD. Notably, the Ru/MgO–Al_2O_3-V catalyst delivers the superior catalytic activity and selectivity,

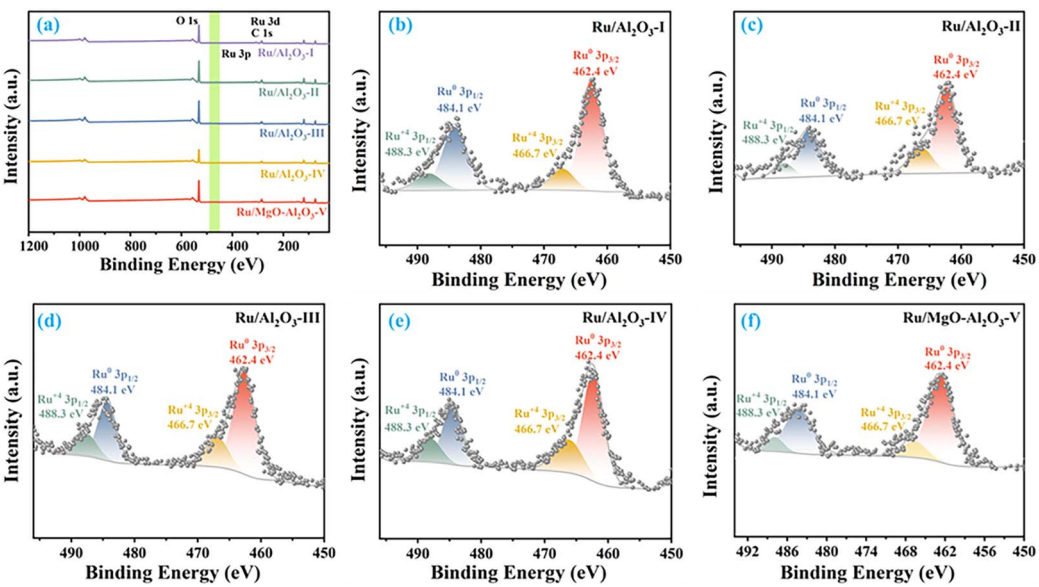

Fig. 5 Wide-scan XPS spectra of the supported ruthenium catalysts. (a) XPS spectra of Ru 3p for the supported ruthenium catalysts: (b) Ru/Al_2O_3-I, (c) Ru/Al_2O_3-II, (d) Ru/Al_2O_3-III, (e) Ru/Al_2O_3-IV and (f) Ru/MgO–Al_2O_3-V.

Table 2 The XPS qualitative analysis of the supported ruthenium catalysts

Catalyst	Ru	Ru $3p_{3/2}$ peak area	Ru $3p_{3/2}$ Ru (0)/Ru (IV)	Ru $3p_{1/2}$ peak area	Ru $3p_{1/2}$ Ru (0)/Ru (IV)
Ru/Al_2O_3-I	Ru (0)	8535.31	4.87	5512.45	4.06
	Ru (IV)	1751.77		1357.75	
Ru/Al_2O_3-II	Ru (0)	4910.4	3.05	2833.96	3.78
	Ru (IV)	1608.56		750.36	
Ru/Al_2O_3-III	Ru (0)	5841.16	3.18	2860.97	2.96
	Ru (IV)	1834.01		966.55	
Ru/Al_2O_3-IV	Ru (0)	9808.47	2.40	5073.69	2.19
	Ru (IV)	4090.98		2320.92	
$Ru/MgO–Al_2O_3$-V	Ru (0)	4809.22	5.97	2553.98	4.93
	Ru (IV)	806.07		518.12	

accompanied by the minimal formation of byproducts from C–C and C–OH bond cleavage. Conversely, the catalysts without NaOH treatment (Ru/Al_2O_3-I and Ru/Al_2O_3-II) show the highest yield of such cleavage-derived byproducts. Collectively, optimization of the preparation protocol and MgO modification not only promotes the formation of highly dispersed ultrasmall Ru nanoparticles but also modulates the catalyst's acid–base properties, thereby enhancing catalytic activity, suppressing side reactions, and ultimately improving the overall catalytic performance.

In this study, a high-performance $Ru/MgO–Al_2O_3$-V hydrogenation catalyst is developed, which delivers exceptional catalytic performance in *o*-cresol hydrogenation. The catalyst features robust aromatic ring saturation activity while efficiently suppressing C–C and C–OH bond cleavage, thus holding substantial application potential. Herein, aromatic compounds with diverse functional groups are utilized as substrates to assess the catalyst's performance, with the results compiled in Table 4. As clearly reflected in the data, the catalyst exhibits outstanding catalytic efficacy in the hydrogenation of other aromatic compounds bearing varied functional groups—particularly for bisphenol-type compounds, where it shows remarkable effectiveness in inhibiting C–OH bond cleavage, and the selectivity toward the target products in the hydrogenation of hydroquinone and bisphenol A both exceeds 98.5% (Entry 1, 2). Additionally, the catalyst demonstrates high selectivity exclusively toward aromatic ring saturation, irrespective of the presence of aldehyde, ester, ether, or nitrile moieties on the aromatic ring (Entry 3,5–7). Furthermore, the catalyst's catalytic performance in the hydrogenation of biomass-derived furan compounds is further explored. Intriguingly, it also displays favorable furan ring hydrogenation capability (Entry 3). Across all the investigated hydrogenation reactions, the catalyst sustains strong aromatic/furan ring saturation activity while suppressing the hydrogenolysis and hydrogenation of functional groups, including C–C, C–O–C, C–OH, –CHO, –C═O, and –CN. The optimization of the catalyst preparation protocol and MgO modification are the pivotal factors underpinning the catalyst's exceptional performance.

3.3 Proposed reaction mechanism

From above observations, it can be summarized that a novel $Ru/MgO–Al_2O_3$ catalyst with highly dispersed ultra-small nanoparticles for aromatic selective hydrogenation was developed *via* precise precursor design and optimization. The Ru/MgO–

Table 3 Catalytic performance for *o*-cresol hydrogenation over synthesized catalysts [a]

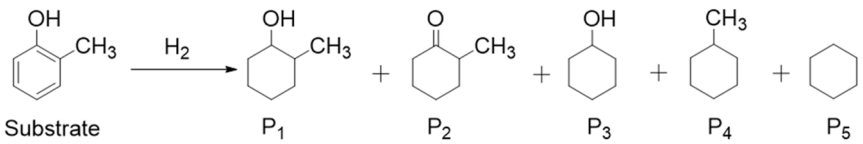

Catalysts	Conv. (%)	Product distribution (% selectivity) P1	P2	P3	P4	P5
Ru/Al_2O_3-I	92.42	82.41	0.63	1.95	10.19	4.82
Ru/Al_2O_3-II	86.39	85.37	0.86	1.60	7.86	4.31
Ru/Al_2O_3-III	98.67	90.63	0.27	1.06	5.48	2.56
Ru/Al_2O_3-IV	85.86	92.49	0.32	0.83	4.19	2.17
$Ru/MgO–Al_2O_3$-V	100.00	99.74	0.01	0.05	0.12	0.08

[a] Reaction conditions: catalyst (15 g), temperature (120 °C), H_2 (5.0 MPa), H/O (Mol) = 6 : 1, WHSV (0.30 h^{-1}), ethanol used as solvent, *o*-cresol concentration 20 wt.%. Products were quantified by GC.

Table 4 Exploration of the universality of the Ru/MgO–Al_2O_3-V[a]

Entry	Substrate	Product	Reaction conditions	Conv. (%)	Sel, (%)
1[b]			100 °C, 0.35 h^{-1}	100.00	98.52
2[c]	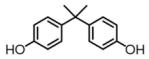	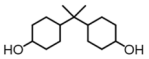	120 °C, 0.3 h^{-1}	100.00	98.53
3[b]	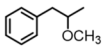	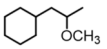	120 °C, 0.3 h^{-1}	100.00	99.76
4[b]			100 °C, 0.35 h^{-1}	100.00	99.16
5[e]	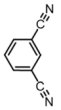	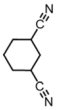	120 °C, 0.15 h^{-1}	100.00	96.84
6[e]	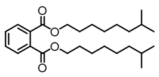	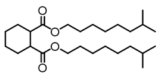	120 °C, 0.2 h^{-1}	100.00	99.52
7[e]	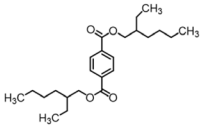	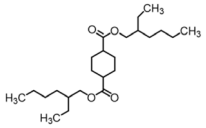	120 °C, 0.2 h^{-1}	100.00	99.48

[a] Reaction conditions: catalyst (15 g), H_2 (5.0 MPa), H/O (mol) = ([b,d,e] 6 : 1,[c] 10 : 1), substrate concentration (20 wt.%), solvent ([b] ethanol, [c,d] isopropanol, [e] isooctanol). Products were quantified by GC.

Al_2O_3 catalyst enables highly selective aromatic ring hydrogenation while suppressing C–C, C–OH and others bond hydrogenolysis. The proposed reaction mechanism is illustrated in Fig. 6. As can be observed from the selective hydrogenation of o-cresol to *o*-methylcyclohexanol, catalysts synthesized *via* different methods show distinct catalytic activity and selectivity. Notably, the exceptional hydrogenation activity of the optimal catalyst originates from highly dispersed active Ru centers and the formation of ultra-small Ru nanoparticles (minimum size: 1.72 nm). Analysis of hydrogenation products indicates that MgO-free catalysts with relatively strong acidity produce more by-products, attributed to C–O and C–C bond cleavage. In contrast, the Ru/MgO–Al_2O_3 catalyst exhibits a more prominent ability to suppress such bond cleavage. Further studies confirm that the Ru/MgO–Al_2O_3 catalyst enables efficient aromatic ring hydrogenation for aromatic compounds bearing various benzene-attached functional groups, while also effectively inhibits the hydrogenolysis of such functional groups (*e.g.*, C–C, C–O) on the aromatic ring. Overall, the proposed reaction mechanism might be the modification by MgO resulted in changes in their electronic properties, which enhance the adsorption of phenolics and ultimately resulted in superior catalytic activity. Furthermore, the acidity regulation by MgO reduced catalyst's acidic sites, not only enhanced the dispersion of active ruthenium species and facilitated the formation of ultra-small Ru nanoparticles but also inhibits the cleavage of C–OH, C–C and others bonds under acidic environments. Ultimately, this synergistic effect enabled the development of the aromatic compounds hydrogenation catalyst with outstanding activity and selectivity.

3.4 Catalytic stability

A kiloton-scale production unit for *o*-methylcyclohexanol has been successfully established. A long-term catalytic stability test (Fig. 7) was conducted under optimal reaction conditions, where the Ru/MgO–Al_2O_3-V catalyst operated continuously in industrial equipment more than 4000 hours. Throughout the test, *o*-cresol conversion remained above 99.96%, while the selectivity towards the target product *o*-methylcyclohexanol is stably maintained at over 99.5%. Additionally, HPLC analysis revealed that residual *o*-cresol in the hydrogenation products is consistently below 400 ppm. These results confirm the catalyst's excellent stability and suitability for long-term service in continuous fixed-bed reactors. Notably, prior studies[58] demonstrated that MgO can enhance the electron cloud density around active metal sites (*e.g.*, Ni) and effectively suppress catalyst coking and poisoning. For the Ru/MgO–Al_2O_3-V catalyst, its outstanding catalytic performance is closely associated with MgO modification. This modification not only facilitates the formation of highly dispersed ultra-small Ru nanoparticles but also reduces the catalyst's acidity. The diminished acidity inhibits the cleavage of C–OH and C–C bonds, which leads to the formation of various hydrogenation by-products—thereby significantly improving the selectivity towards the target product.

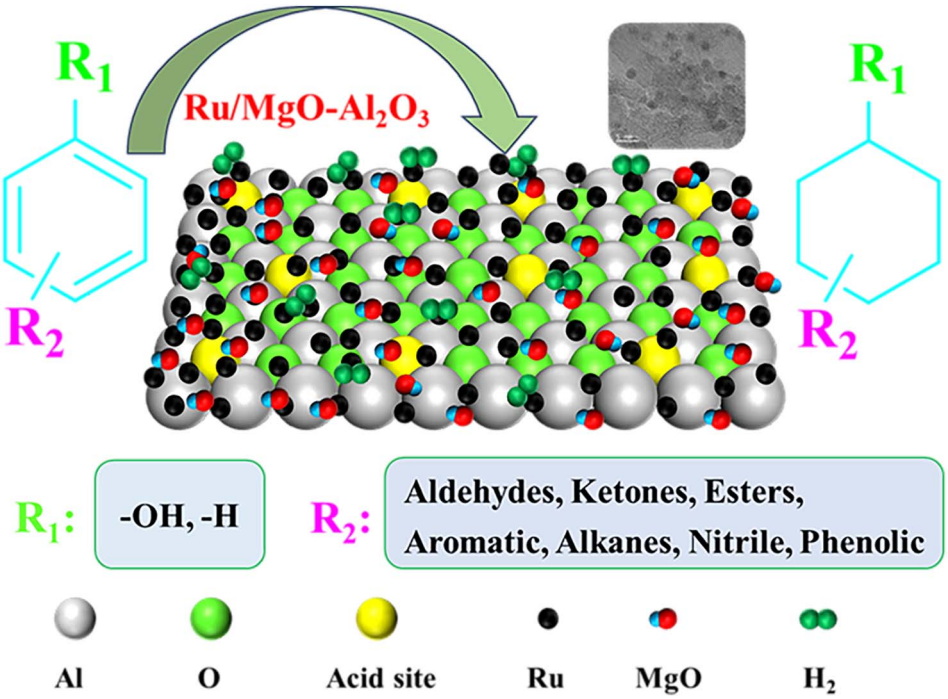

Fig. 6 Proposed reaction mechanisms for aromatic compounds hydrogenation over Ru/MgO–Al_2O_3 catalyst.

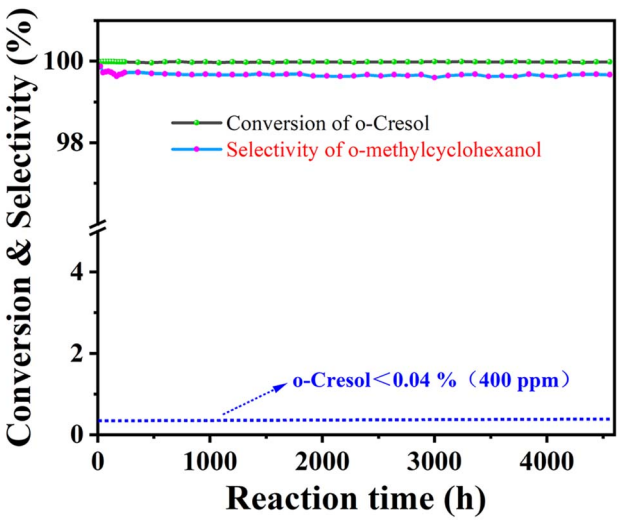

Fig. 7 Stability of Ru/MgO–Al_2O_3-V catalyst. Reaction conditions: the amount of catalyst 500 kg, ethanol used as solvent, *o*-Cresol concentration 20 wt.%. H_2 4.0–5.0 MPa, H/O (mol) 6–10 : 1, reaction temperature 115–135 °C, WHSV 0.25–0.45 h^{-1}.

4. Conclusion

A novel heterogeneous Ru-based catalyst featuring highly dispersed ultra-small Ru nanoparticles was successfully fabricated. This catalyst delivers exceptional catalytic performance in the continuous fixed-bed hydrogenation of *o*-cresol to *o*-methylcyclohexanol. Furthermore, investigations demonstrate that the catalyst also delivers outstanding performance in the hydrogenation saturation of other aromatic compounds while suppressing the hydrogenolysis and hydrogenation of functional groups, irrespective of the presence of aldehyde, ester, ether, or nitrile moieties on the aromatic ring. Overall, tailoring of the catalyst synthesis route and MgO modification stand as the pivotal elements responsible for the outstanding catalytic performance. In particular, MgO modification promotes the homogeneous dispersion of active centers, the formation of ultra-small Ru nanoparticles, and the precise fine-tuning of acid-base properties—thereby suppressing the generation of undesirable side reactions and highlighting its considerable potential for industrial implementation.

Author contributions

Yongjun Wang: conceptualization, data curation, writing – original draft, investigation, project administration, validation, visualization. Cheng Han: conceptualization, methodology, formal analysis, investigation, writing – review and editing, Funding acquisition. Xiaohan Wu: formal analysis, investigation, visualization. Minglin Xiang: investigation, project administration, resources, funding acquisition. Tao Liu: formal analysis, investigation, visualization. Xiaoshan Zhang: formal analysis, supervision, validation. Bing Wang: methodology, formal analysis, supervision, validation. Yingde Wang: conceptualization, supervision, methodology, formal analysis, investigation, writing – review and editing, funding acquisition.

Conflicts of interest

There are no conflicts to declare.

Data availability

All data generated or analyzed in this study are included in this article.

Supplementary information (SI) is available. See DOI: https://doi.org/10.1039/d5ra08531d.

Acknowledgements

This work was financially supported by the National Natural Science Foundation of China (No. 52202031), the National Key R&D Program (Grant 2021YFC3001103) and the Hunan Provincial Key R&D Project (No. 2023GK2076).

References

1 W. Jiang, J.-P. Cao, X.-Y. Zhao, T. Xie, C. Zhu, J.-X. Xie, L. Zhao, M. Zhao, Y.-P. Zhao and J.-L. Zhang, Highly selective aromatic ring hydrogenation of lignin-derived compounds over macroporous Ru/Nb_2O_5 with the lost acidity at room temperature, *Fuel*, 2020, **282**, 118869, DOI: 10.1016/j.fuel.2020.118869.

2 A. Sreenavya, A. Sahu and A. Sakthwel, Hydrogenation of Lignin-Derived Phenolic Compound Eugenol over Ruthenium-Containing Nickel Hydrotalcite-Type Materials, *Ind. Eng. Chem. Res.*, 2020, **59**, 11979–11990, DOI: 10.1021/acs.iecr.0c01106.

3 X. J. Cui, A. E. Surkus, K. Junge, C. Topf, J. Radnik, C. Kreyenschulte and M. Beller, Highly selective hydrogenation of arenes using nanostructured ruthenium catalysts modified with a carbon-nitrogen matrix, *Nat. Commun.*, 2016, **7**, 11326, DOI: 10.1038/ncomms11326.

4 A. Shundo, S. Yamamoto and K. Tanaka, Network Formation and Physical Properties of Epoxy Resins for Future Practical Applications, *JACS Au*, 2022, **2**, 1522–1542, DOI: 10.1021/jacsau.2c00120.

5 W. Q. Zhan, W. F. Tang, X. L. Shen, H. Xu and J. Zhang, Exposure to bisphenol A and its analogs and polycystic ovarian syndrome in women of childbearing age: A multicenter case-control study, *Chemosphere*, 2023, **313**, 137463, DOI: 10.1016/j.chemosphere.2022.137463.

6 W.-Y. Lu, S. Bhattacharjee, B.-X. Lai, A.-B. Duh, P.-C. Wang and C.-S. Tan, Hydrogenation of Bisphenol A-Type Epoxy Resin (BE186) over Vulcan XC72-Supported Rh and Rh–Pt Catalysts in Ethyl Acetate-Containing Water, *Ind. Eng. Chem. Res.*, 2019, **58**, 16326–16337, DOI: 10.1021/acs.iecr.9b02583.

7 M. Bilal, H. M. N. Iqbal and D. Barceló, Mitigation of bisphenol A using an array of laccase-based robust bio-catalytic cues – A review, *Sci. Total Environ.*, 2019, **689**, 160–177, DOI: 10.1016/j.scitotenv.2019.06.403.

8 X. X. Han, R. J. Zhao, Y. Tian, Y. T. Li, X. W. Chen, J. P. Ma, W. L. Wang, Y. F. Zhang, S. Geng and M. L. Liu, Simple high-performance liquid chromatography-ultraviolet method for simultaneous separation and detection of 14 bisphenol pollutants in building materials, *J. Sep. Sci.*, 2023, **46**, 2300006, DOI: 10.1002/jssc.202300006.

9 J. Piekutin, U. Kotowska, M. Puchlik, W. Polinska and A. Dobkowska, Application of an integrated process for the removal of organic compounds of the phenols group from water, *Desalin Water Treat.*, 2023, **301**, 63–70, DOI: 10.5004/dwt.2023.29659.

10 Y. Saab, E. Oueis, S. Mehanna, Z. Nakad, R. Stephan and R. S. Khnayzer, Risk Assessment of Phthalates and Their Metabolites in Hospitalized Patients: A Focus on Di- and Mono-(2-ethylhexyl) Phthalates Exposure from Intravenous Plastic Bags, *Toxics*, 2022, **10**, 357, DOI: 10.3390/toxics10070357.

11 S. Simar-Mentières, F. Nesslany, M. L. Sola, S. Mortier, J. M. Raimbault, F. Gondelle, L. Chabot, P. Pandard, D. Wils and A. Chentouf, Toxicology and Biodegradability of a Phthalate-Free and Bio-Based Novel Plasticizer, *J. Toxicol.*, 2021, **2021**(1), 9970896, DOI: 10.1155/2021/9970896.

12 Y. Sjöström, K. Hagström, C. Lindh, I. L. Bryngelsson, M. Larsson and J. Hagberg, Exposure to phthalates and DiNCH among preschool children in Sweden: Urinary metabolite concentrations and predictors of exposure, *Int. J. Hyg. Environ. Health*, 2023, **250**, 114163, DOI: 10.1016/j.ijheh.2023.11416.

13 F. M. Akwi and P. Watts, Continuous flow chemistry: where are we now? Recent applications, challenges and limitations, *Chem. Commun.*, 2018, **54**, 13894–13928, DOI: 10.1039/c8cc07427e.

14 Q. J. Fu, H. M. Jiang, Y. J. Wang, H. Y. Wang and X. B. Zhao, Recent advances in metal-organic framework based heterogeneous catalysts for furfural hydrogenation reactions, *Mater. Chem. Front.*, 2023, **7**, 628–642, DOI: 10.1039/D2QM01181F.

15 T. Yin, Y. Ye, H. Jiang, C. Lin, R. Shu, Z. Tian, C. Wang and N. Shi, Efficient Hydrodeoxygenation of Lignin-Derived Phenolic Compounds Over Ru-Based Catalyst with Biochar and Al_2O_3 as Composite Support, *ChemSusChem*, 2024, **18**(1), e202401870, DOI: 10.1002/cssc.202401870.

16 V. O. O. Gonçalves, P. M. de Souza, T. Cabioc'h, V. T. da Silva and F. Richard, Hydrodeoxygenation of m-cresol over nickel and nickel phosphide based catalysts. Influence of the nature of the active phase and the support, *Appl. Catal. B: Environ.*, 2017, **219**, 619–628, DOI: 10.1016/j.apcatb.2017.07.042.

17 E. V. Ilyina, D. V. Yurpalova, D. A. Shlyapin, G. B. Veselov, D. M. Shivtsov, V. O. Stoyanovskii, A. V. Bukhtiyarov and A. A. Vedyagin, Effect of preparation conditions of nanocrystalline Pd/MgO catalysts on their performance in selective hydrogenation of acetylene, *Mol Catal.*, 2024, **560**, 114151, DOI: 10.1016/j.mcat.2024.114151.

18 Y. Zhang, W. Wei, C. Wang, D. Zhang, H. Li, D. Zhang and Y. Zhang, Preparation of ultrathin two-dimensional nanosheet Ni/TiO2-SC catalyst and their catalytic performance in the liquid-phase hydrogenation of maleic anhydride, *J. Super Crit. Fluids*, 2025, **221**, 106573, DOI: 10.1016/j.supflu.2025.106573.

19 Z. Yang, Q. Qi, M. Fan, Y. Wang and L. Tong, Effects of the preparation methods of Co_3O_4 catalysts on catalytic

oxidization performance toward *o*-xylene, *Mol Catal.*, 2025, **579**, 115095, DOI: 10.1016/j.mcat.2025.115095.

20 X. Y. Bian, H. L. An, X. Q. Zhao and Y. J. Wang, Size effect of Rh/γ-Al_2O_3 catalyst in selective hydrogenation of dimethyl toluene-2,4-dicarbamate, *Appl. Catal. A: Gen.*, 2025, **702**, 120336, DOI: 10.1016/j.apcata.2025.120336.

21 Y. Liu, D. Liu, J. Zhang, Z. Qu, Y. Du, Z. Tang, H. Jiang, W. Xing and R. Chen, Easily Recyclable Pd@CN/SiNFs Catalysts for Efficient Phenol Hydrogenation, *Ind. Eng. Chem. Res.*, 2025, **64**, 5313–5325, DOI: 10.1021/acs.iecr.4c04904.

22 Q. Long, C. Shi, D. Zhang, D. Wei, H. Li, L. Zhou, H. Tan, J. Yu and M. Xu, The synthesis of PtCu/C catalyst with a hollow sphere structure by chlorine-free platinum precursor for the oxygen reduction reaction, *Int. J. Hydrog. Energy*, 2025, **133**, 214–224, DOI: 10.1016/j.ijhydene.2025.04.487.

23 T. W. Kim, H.-J. Chun, Y. Jo, D. Kim, H. Ko, S. H. Kim, S. K. Kim and Y.-W. Suh, Electronic vs. Geometric effects of Al_2O_3-supported Ru species on the adsorption of H_2 and substrate for aromatic LOHC hydrogenation, *J. Catal.*, 2023, **428**, 115178, DOI: 10.1016/j.jcat.2023.115178.

24 V. K. Velisoju, G. B. Peddakasu, N. Gutta, V. Boosa, M. Kandula, K. V. R. Chary and V. Akula, Influence of Support for Ru and Water Role on Product Selectivity in the Vapor-Phase Hydrogenation of Levulinic Acid to γ-Valerolactone: Investigation by Probe-Adsorbed Fourier Transform Infrared Spectroscopy, *J. Phys. Chem. C*, 2018, **122**, 19670–19677, DOI: 10.1021/acs.jpcc.8b06003.

25 A. Bermejo-López, B. Pereda-Ayo, J. A. Onrubia-Calvo, J. A. González-Marcos and J. R. González-Velasco, Enhancement of the CO_2 adsorption and hydrogenation to CH_4 capacity of Ru–Na–Ca/γ–Al_2O_3 dual function material by controlling the Ru calcination atmosphere, *J. Environ. Sci.*, 2024, **140**, 292–305, DOI: 10.1016/j.jes.2023.08.041.

26 T. Vandevyvere, M. K. Sabbe, P. S. F. Mendes, J. W. Thybaut and J. Lauwaert, NiCu-based catalysts for the low-temperature hydrodeoxygenation of anisole: Effect of the metal ratio on SiO_2 and γ-Al_2O_3 supports, *Green Carbon*, 2023, **1**, 170–184, DOI: 10.1016/j.greenca.2023.10.001.

27 B. Wang, L. Li, T. Zhang, J. Wu and J. Zhang, Janus-Ligand-Engineered High-Performance Single-Atom Ru Catalyst for Acetylene Hydrochlorination, *ACS Catal.*, 2025, **15**, 3085–3095, DOI: 10.1021/acscatal.4c07372.

28 S. Zhou, L. Wang, S. Gao, X. Chen, C. Zhang, D. Yu, X. Fan, X. Yu and Z. Zhao, Research Progress on Preparation of Metal Oxide Catalysts with Porous Structure and Their Catalytic Purification of Diesel Engine Exhausts Gases, *ACS Catal.*, 2024, **14**, 6062–6127, DOI: 10.1021/acscatal.4c00323.

29 Z. Rong, W. Shen and Y. Fang, Alkaline earth modified activated carbon supported Cu catalysts with enhanced selectivity in the hydrogenation of dimethyl oxalate to methyl glycolate, *RSC Adv.*, 2024, **14**, 11849–11861, DOI: 10.1039/D4RA01049C.

30 V. Nori, H. A. Sidi and M. Nielsen, Selective hydrogenation of HMF to DHMF with Ru–PNP complexes in ionic liquids, *RSC Adv.*, 2025, **15**, 12791–12796, DOI: 10.1039/D5RA01002K.

31 Y. Wang, C. Han, Z. Fu, M. Xiang, T. Liu, X. Zhang, Y. Ou, S. Zhang, B. Wang and Y. Wang, Ultra-small Ru nanoparticles supported on MgO modified Al_2O_3 for efficient selective hydrogenation of hydroquinone to 1,4-cyclohexanediol, *Appl. Catal. O: Open.*, 2025, **206**, 207058, DOI: 10.1016/j.apcato.2025.207058.

32 L. Zuo, J. Cai, Z. Guo, Y. Fu and J. Shen, Effect of amine group on the hydrogenation of aromatic rings over Ru/MgO-Al_2O_3 catalysts, *Chem. Commun.*, 2022, **170**, 106496, DOI: 10.1016/j.catcom.2022.106496.

33 J. Kim, D. Kim, B. G. Park, D. Oh, S. Lee, J. Kim, E. Nam and K. An, Effective production of liquid/wax fuels from polyethylene plastics using Ru/Al_2O_3 catalysts, *EES Catal.*, 2025, **3**, 822–831, DOI: 10.1039/d5ey00070j.

34 C. Sui, F. Yuan, Z. Zhang, C. Zhang, X. Niu and Y. Zhu, Effect of Ru Species on N_2O Decomposition over Ru/Al_2O_3 Catalysts, *Catalysts*, 2016, **6**(11), 173, DOI: 10.3390/catal6110173.

35 W. Kim, K. Y. Koo, H. J. Lee, Y. G. Shul and W. L. Yoon, Highly dispersed nickel catalyst promoted by precious metals for CO selective methanation, *Int. J. Hydrog. Energy.*, 2015, **40**, 10033–10040, DOI: 10.1016/j.ijhydene.2015.06.033.

36 X. X. Wang, M. Chen, X. X. Qin, B. L. Li, X. Y. Chen, J. H. Zhang, K. L. Li and C. B. Zhang, Enhanced activity of CO oxidation at room temperature by tuning the metal-support interaction of Ru/CeO_2 catalyst, *J. Environ. Sci.*, 2025, **154**, 436–443, DOI: 10.1016/j.jes.2024.07.021.

37 H. Fang, S. Wu, T. Ayvali, J. Zheng, J. Fellowes, P.-L. Ho, K. C. Leung, A. Large, G. Held, R. Kato, K. Suenaga, Y. I. A. Reyes, H. V. Thang, H.-Y. T. Chen and S. C. E. Tsang, Dispersed surface Ru ensembles on MgO(111) for catalytic ammonia decomposition, *Nat. Commun.*, 2023, **14**(1), 647, DOI: 10.1038/s41467-023-36339-w.

38 Y. H. Yue, J. Tian, J. Ma, S. Yang, W. Li, J. L. Huang, Q. B. Li and G. W. Zhan, Regulation of acidity properties of ZSM-5 and proximity between metal oxide and zeolite on bifunctional catalysts for enhanced CO_2 hydrogenation to aromatics, *Appl. Catal. B: Environ.*, 2024, **355**, 124158, DOI: 10.1016/j.apcatb.2024.124158.

39 Y. Y. Chen, T. L. Lu, X. M. Yang and L. P. Zhou, Regulation of acid/basic properties of Zr-Beta zeolite for efficient conversion of furfural to furfuryl alcohol, *Mol. Catal.*, 2024, **559**, 114093, DOI: 10.1016/j.mcat.2024.114093.

40 A. Srifa, M. Kalong, W. Praikaew, S. Ratchahat, W. Chaiwat, W. Koo-Amornpattana, W. Klysubun, W. Limphirat, S. Assabumrungrat and S. Kawi, Regulation of Pt Loading on Co/Al_2O_3 Catalysts for Selective Hydrogenation and Hydrogenolysis of 5-Hydroxymethylfurfural to 2,5-Bis(hydroxymethyl)furan and 2,5-Dimethylfuran, *ChemCatChem*, 2024, **16**, e202301360, DOI: 10.1002/cctc.202301360.

41 J. G. Yang, J. X. Feng, Y. P. Cao, Y. X. Xiao, L. L. Qiao, K. Y. An, J. Yang, J. Peng, H. Pan and H. M. Cheng, Highly Dispersed Ru-Pt Heterogeneous Nanoparticles on Reduced Graphene Oxide for Efficient pH-Universal Hydrogen Evolution, *Adv. Funct. Mater.*, 2024, **34**, 1, DOI: 10.1007/s42114-022-00452-z.

42 Y. Yan, Y. Han, D. Li, J. Huang and Q. Lian, Effect of $NaAlO_2$ concentrations on microstructure and corrosion resistance of Al_2O_3/ZrO_2 coatings formed on zirconium by micro-arc oxidation, *Appl. Sur. Sci.*, 2010, **256**, 6359–6366, DOI: 10.1016/j.apsusc.2010.04.017.

43 Y. Zhou, D. Ye, Y. Wu, C. Zhang, W. Bai, Y. Tian and M. Qin, Low-cost preparation and characterization of $MgAl_2O_4$ ceramics, *Ceram. Inter.*, 2022, **48**, 7316–7319, DOI: 10.1016/j.ceramint.2021.11.196.

44 S. Ramesh, K. Indukuri, O. Riant and D. P. Debecker, Synthesis of Carbonate Esters by Carboxymethylation Using $NaAlO_2$ as a Highly Active Heterogeneous Catalyst, *Org. Process Res. Dev.*, 2018, **22**, 1846–1851, DOI: 10.1021/acs.oprd.8b00333.

45 Y. Park, H. Ku, J.-Y. An, J. Han, C.-H. Shin and J.-K. Jeon, Effect of MgO promoter on Ru/γ-Al_2O_3 catalysts for tricyclopentadiene hydrogenation, *Catal. Today*, 2020, **352**, 308–315, DOI: 10.1016/j.cattod.2020.01.003.

46 Y.-X. Fu, S.-Y. Huang, M.-S. Sun, Y. Zhou, D.-D. Cai, W.-S. Zhu, W. Hui and D.-J. Tao, Ambient-temperature α-pinene hydrogenation to cis-pinane over Ru/CeO_2-H catalyst via the dimethyl-up configuration, *Chem. Eng. J.*, 2025, **512**, 162563, DOI: 10.1016/j.cej.2025.162563.

47 D. Fu, X. Wu, B. Cui, Y. Guo, H. Wang, J. Han, Q. Ge and X. Zhu, $Ru_{0.05}Ce_{0.95}O_2$ Solid Solution Derived Ru Catalyst Enables Selective Hydrodeoxygenation of m-Cresol to Toluene, *ChemCatChem*, 2021, **13**, 4814–4823, DOI: 10.1002/cctc.202101239.

48 V. Mazzieri, F. Coloma-Pascual, A. Arcoya, P. C. L'Argenti`ere, x F1 and N. S. goli, XPS, FTIR and TPR characterization of Ru/Al_2O_3 catalysts, *Appl. Surf. Sci.*, 2003, **210**(3), 222–230, DOI: 10.1016/S0169-4332(03)00146-6.

49 S. Cisneros, L. Santa-Taborda, L. Martínez Quintana, A. I. M. Rabee, H. Abed, N. Rockstroh, S. Bartling, M. Romero-Sáez, H. Atia, A. Belén Dongil, A. Brückner and J. Rabeah, The effect of O-vacancies on intermediates stability and electron delocalization over MgO modified Ru/ZrO_2: Spectroscopic insights during CO_2 methanation, *Chem. Eng. J.*, 2023, **474**, 145646, DOI: 10.1016/j.cej.2023.145646.

50 S. Zhang, C. Zhao, Y. I. A. Reyes, P. Xiong, T. Chen, T. Cheng, X. Yi, S.-W. Chou, C.-Y. Chien, Y.-Y. Yang, J. L. Chen, T. W. B. Lo, M. M.-J. Li, H.-Y. T. Chen, A. Zheng and Y.-K. Peng, Facile Gram-Scale Synthesis of Size-Tunable MgO Nanosheets Enclosed by (111) Surface with Remarkable Stability and Uniform Host Sites for Atom Dispersion, *Chem. Mater.*, 2024, **36**, 4204–4214, DOI: 10.1021/acs.chemmater.3c03018.

51 V. K. Velisoju, G. B. Peddakasu, N. Gutta, V. Boosa, M. Kandula, K. V. R. Chary and V. Akula, Influence of Support for Ru and Water Role on Product Selectivity in the Vapor-Phase Hydrogenation of Levulinic Acid to γ-Valerolactone: Investigation by Probe-Adsorbed Fourier Transform Infrared Spectroscopy, *J. Phys. Chem. C*, 2018, **122**, 19670–19677, DOI: 10.1021/acs.jpcc.8b06003.

52 W. Luo, P. C. A. Bruijnincx and B. M. Weckhuysen, Selective, one-pot catalytic conversion of levulinic acid to pentanoic acid over Ru/H-ZSM5, *J. Catal.*, 2014, **320**, 33–41, DOI: 10.1016/j.jcat.2014.09.014.

53 L. Zhang, M. Zhou, A. Wang and T. Zhang, Selective Hydrogenation over Supported Metal Catalysts: From Nanoparticles to Single Atoms, *Chem. Rev.*, 2019, **120**, 683–733, DOI: 10.1021/acs.chemrev.9b00230.

54 Z. H. Ouyang, G. Sheng, Y. Zhong, J. Wang, J. X. Cai, S. G. Deng and Q. Deng, Palladium Single Atom-supported Covalent Organic Frameworks for Aqueous-phase Hydrogenative Hydrogenolysis of Aromatic Aldehydes via Hydrogen Heterolysis, *Angew. Chem., Int. Ed.*, 2025, **64**(6), e202418790, DOI: 10.1002/anie.202418790.

55 H. Li, D. Ji, Y. Li, Y. Liang and G. X. Li, Effect of alkaline earth metals on the liquid-phase hydrogenation of hydroquinone over Ru-based catalysts, *Solid State Sci.*, 2015, **50**, 85–90, DOI: 10.1016/j.solidstatesciences.2015.10.014.

56 J. G. Yang, J. X. Feng, Y. P. Cao, Y. X. Xiao, L. L. Qiao, K. Y. An, J. Yang, J. Peng, H. Pan and H. M. Cheng, Highly Dispersed Ru-Pt Heterogeneous Nanoparticles on Reduced Graphene Oxide for Efficient pH-Universal Hydrogen Evolution, *Adv. Funct. Mater.*, 2024, **34**, e202201132, DOI: 10.1002/cctc.202201132.

57 A. Heidari, K. D. Safa and R. Teimuri-Mofrad, Chlorophyll b-modified TiO_2 nanoparticles for visible-light-induced photocatalytic synthesis of new tetrahydroquinoline derivatives, *Mol Catal.*, 2023, **547**, 113338, DOI: 10.1016/j.mcat.2023.113338.

58 S. Zhang, C. Zhao, Y. I. A. Reyes, P. Xiong, T. Chen, T. Cheng, X. Yi, S.-W. Chou, C.-Y. Chien, Y.-Y. Yang, J. L. Chen, T. W. B. Lo, M. M.-J. Li, H.-Y. T. Chen, A. Zheng and Y.-K. Peng, Facile Gram-Scale Synthesis of Size-Tunable MgO Nanosheets Enclosed by (111) Surface with Remarkable Stability and Uniform Host Sites for Atom Dispersion, *Chem. Mater.*, 2024, **36**, 4204–4214, DOI: 10.1021/acs.chemmater.3c03018.